Potential-induced sonoelectrochemical graphene nanosheets with vacancies as hydrogen peroxide reduction catalysts and sensors

Tzu-Pei Wang [a], Chien-Liang Lee [a,*], Chia-Hung Kuo [b], Wen-Cheng Kuo [c]

[a] *Department of Chemical and Materials Engineering, National Kaohsiung University of Science and Technology, Kaohsiung 807, Taiwan*
[b] *Department of Seafood Science, National Kaohsiung University of Science and Technology, Kaohsiung, Taiwan*
[c] *Department of Mechatronics Engineering, National Kaohsiung University of Science and Technology, Kaohsiung, Taiwan*

ABSTRACT

Defective graphene nanosheets (dGN_{4V}) with 5-9, 5-8-5, and point defects were synthesised by a sonoelectrochemical method, where a potential of 4 V (vs. Ag/AgCl) was applied to drive the rapid intercalation of phosphate ions between the layers of the graphite foil as a working electrode. In addition to these vacancies, double vacancy defects were also created when the applied potential was increased to 8 V (dGN_{8V}). The defect density of dGN_{8V} (2406 μm^{-2}) was higher than that of dGN_{4V} (1786 μm^{-2}). Additionally, dGN_{8V} and dGN_{4V} were applied as catalysts for the hydrogen peroxide reduction reaction (HPRR). The mass activity of dGN_{8V} (1.31×10^{-2} mA·μg^{-1}) was greater than that of dGN_{4V} (1.17×10^{-2} mA·μg^{-1}) because of its high electrochemical surface area (ECSA, 1250.89 $m^2 \cdot g^{-1}$) and defect density (N_D, 2406 μm^{-2}), leading to low charge transfer resistance on the electrocatalytic interface. The ECSA and N_D of dGN_{4V} were 502.7 $m^2 \cdot g^{-1}$ and 1786 μm^{-2}, respectively. Apart from its remarkable HPRR activity, the cost-effective dGN_{8V} catalyst also showed potential as an amperometric sensor for the determination of H_2O_2.

1. Introduction

Graphene nanosheets with vacancy defects (defective graphene nanosheet, dGN) can be a source of numerous active sites within the vacancies; these can effectively promote electrocatalytic reactions when dGN is directly used as a catalyst. The high activities of defective graphene with pentagon, 5-8-5, and 5-7-7-5 vacancies were evaluated for hydrogen evolution, oxygen reduction, and oxygen evolution reactions because these vacancies can lower the activation barrier [1]. The overpotential of reduced graphene oxide with double vacancies is almost equal to that of metal-based catalysts [2]; thus, carbon catalysts with vacancy defects showed large faradaic efficiency and high production rates for NH_3 in the N_2 reduction reaction [2]. Its remarkable performance can also be attributed to the high defect density and surface area [3]. In the electrocatalytic reduction of CO_2, dGN can offer abundant catalytically active sites to strongly adsorb CO_2 [4], leading to high faradaic efficiency. An exquisite experiment clearly showed that the electron transfer rate constant in the redox reaction of hydroxymethylferrocene can increase by an order of magnitude with the increase in defect density (N_D) [5]; theoretical calculations also confirmed this correlation [6].

Defective graphene is classically synthesised by physical or chemical methods, such as Ar^+ bombardment [5], elimination of N from N-doped graphene [1,4], and ultrasonication and hydrothermal reaction of graphene oxide (GO) [2]. These methods require expensive equipment or complex processes. The sonoelectrochemical method is a simple one-pot approach to prepare dGN by exfoliation, which occurs because of the fast intercalation of an ion into the layer spacing of a graphite electrode under a synergy of electric field and ultrasonic oscillation. The ultrasound in the electrochemical medium can effectively improve the mass transfer and thin the diffusion layer at the electrode interface [7]. In an earlier study, dGN with a single vacancy was prepared with sodium n-dodecyl sulphate (SDS) as an intercalating agent at an applied potential of ~3 V, oscillation power of 240 W, and oscillation frequency of 37 kHz [8].

In this study, dGNs (dGN_{4V} and dGN_{8V}) with 5-9, 5-8-5, and point defects, respectively, were successfully obtained by the sonoelectrochemical method; the potential applied was 4 or 8 V (vs. Ag/AgCl), and phosphate buffer (PB, pH = 7.4) was used as the electrolyte. In addition to these defects, double vacancies were also created on the dGN_{8V}. The effect of the potential on the properties of the prepared dGNs was studied. Additionally, these two dGNs were applied as

electrocatalysts for the hydrogen peroxide reduction reaction (HPRR), which occurs in hydrogen peroxide fuel cells [9-11] and hydrogen peroxide sensors [12-14]. The sources of their activity as HPRR catalysts and their application as sensors were systematically studied.

2. Materials and methods

2.1. Chemicals and materials

The materials required for the sonoelectrochemical synthesis of dGN_{8V} and dGN_{4V} were graphite plates (Jinglong Special Carbon, 99.99%), sodium dihydrogen phosphate (SHOWA, 98%), and disodium hydrogen phosphate (SHOWA, 99%). GO (>95%) was purchased from Hengqiu Tech Company. The chemicals required for the electrochemical H_2O_2 sensing and measurements were H_2O_2 (Sigma-Aldrich, 35%), D-glucose (Glu, Sigma-Aldrich, 98%), dopamine hydrochloride (DA, Alfa Aesar, 99%), L-ascorbic acid (AA, Sigma-Aldrich, 99.7%), uric acid (UA, Panreac, 98%), KOH (Sigma-Aldrich, 99.99%), isopropanol (OSAKA, 99%), Nafion (Dupont, 5 wt%), milk (FreshDelight), and a standard solution of potassium permanganate (Fisher Chemical, 0.02 M).

2.2. Sonoelectrochemical preparation and materials analysis of dGN

A three-electrode cell was used for the sonoelectrochemical preparation of dGNs containing oxygen groups and vacancies in a 0.1 M PB (pH = 7.4) electrolyte under ultrasonic radiation. The power and frequency of the ultrasonic generator (Elma, P60H) were 640 W and 37 kHz, respectively. Two graphite plates (4 cm × 1 cm × 0.2 cm) were employed as the working and counter electrodes; the distance between them was fixed at 4 cm. To precisely control and maintain the intercalating potential, an Ag/AgCl electrode filled with 3 M KCl solution was used as the reference electrode. All electrodes were connected to a computer-controlled potentiostat (Autolab, PGSTAT 302 N). Fixed potentials of 4 and 8 V were applied for 6 h to prepare dGN_{4V} and dGN_{8V}, respectively. The temperature of the electrolyte was 40 °C.

The as-prepared dGN solution was centrifuged at 9720 × g for 10 min to eliminate the precipitated graphite powders, yielding the purified dGN solution. The dGN powders were obtained by centrifugation of the solution at 34,300 × g for 10 min, followed by freeze drying the precipitate at −80 °C for 3 h.

The morphologies and vacancy defects of the dGNs were examined by transmission electron microscopy (TEM, JEOL JEM-2100) and spherical-aberration corrected field TEM (80 kV, JEOL JEM – ARM200FTH), respectively. Their crystal structures were identified and compared by X-ray diffraction (XRD, Bruker D8). Raman (Horiba HR800, Laser 532 nm) and X-ray photoelectron spectroscopy (XPS, VersaProbe PHI 5000) were used to measure the sp^3/sp^2 ratios and oxygen-containing groups, respectively. The oxygen-containing groups were confirmed using Fourier transform infrared spectroscopy (FTIR, Perkin-Elmer spectrum RX-1). An accelerated surface area and porosimetry system (Micromeritics ASAP2010) was employed for the nitrogen-sorption isotherm experiments.

2.3. Electrocatalysis and electrochemical measurements

Catalysis of HPRR by dGN_{8V}, dGN_{4V}, and GO was performed in a three-electrode cell with various carbon catalyst-coated glassy carbon electrodes (GCE, 0.07 cm^2) as the working electrode, Ag/AgCl (3 M KCl) as the reference electrode, and Pt foil as the counter electrode. All the HPRRs were recorded using a potentiostat. The catalyst inks were prepared by mixing the dried dGN powders (1.75 mg) with a solution of 0.8 mL isopropanol, 1.69 mL deionised water, and 10 μL Nafion solution (5 wt%), and by dispersing them in a vibrating oscillator for 5 min. The GO ink was prepared by mixing 5 mg GO powder, 1 mL deionised water, and 20 μL of 5 wt% Nafion solution. The solid content (0.7 $\mu g \cdot \mu L^{-1}$ or 5 $mg \cdot mL^{-1}$) of the dGN or GO catalysts in the inks was confirmed using a
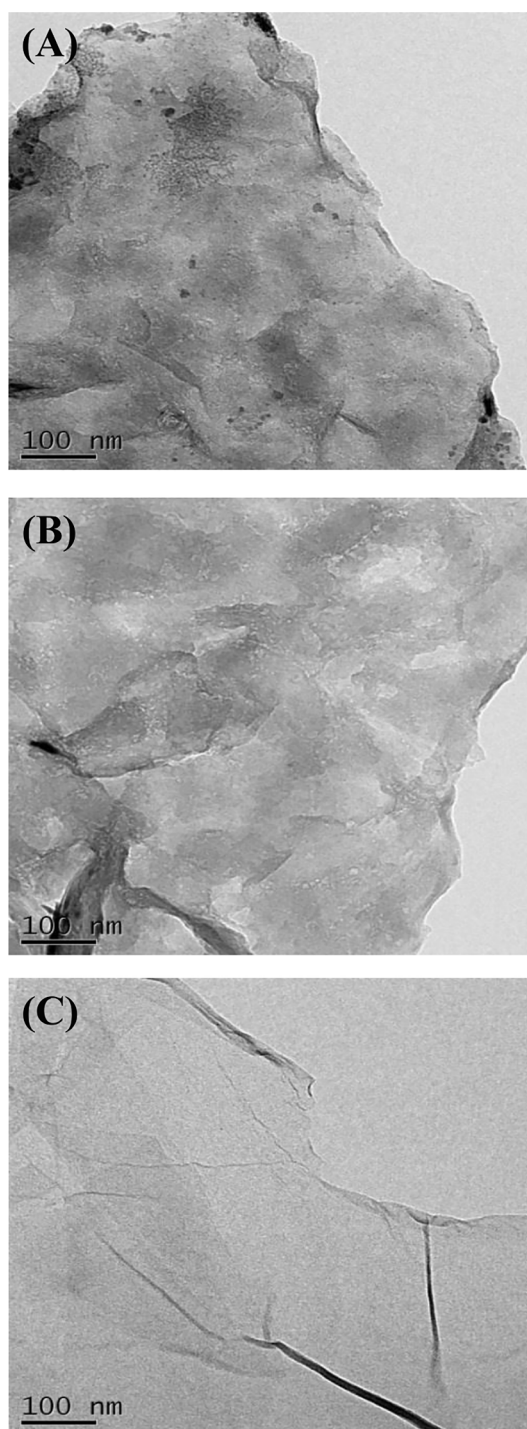

Fig. 1. TEM images of (A) dGN_{8V}, (B) dGN_{4V}, and (C) GO.

quartz crystal microbalance (Seiko QCA 922). The working electrode was prepared by a drop-casting method; the ink (20 μL) was carefully drop-casted onto the GCE surface and dried in a vacuum oven at 30 °C to obtain a uniform layer. To remove potential interference from impurities on the catalyst during HPRR, the working electrode was scanned using cyclic voltammetry (CV) from −0.6 to 0.6 V for three cycles at 150 $mV \cdot s^{-1}$ in an N_2-saturated 0.01 M PB solution. The catalytic properties of dGN and GO were studied using linear scanning voltammetry (LSV) from 0.4 V to −0.6 V for 10 cycles at 10 $mV \cdot s^{-1}$ in N_2-saturated PB solutions (50 mL, 0.01 M, pH = 7.4) with 50 mM H_2O_2. In the same electrolyte, the electrochemical impedance spectra (EIS) for the catalysis of the HPRR were recorded at −0.4 V in the frequency range 100 kHz to

1 mHz. The alternating current amplitude was 10 mV.

The electrochemical surface areas (ECSAs) of dGN_{8V}, dGN_{4V}, and GO were estimated from their double-layer capacitances obtained from CV measurements in 100 mL N_2-saturated 0.1 M KOH solutions from -0.9283 to -0.8283 V (vs. Ag/AgCl) at the rates of 100, 80, 60, 40, 20, and 10 mV·s^{-1}.

To characterise the electrochemical sensing of H_2O_2, the sensitivity, interference, and real sample studies were investigated using chronoamperometric HPRR experiments, where a potential of -0.4 V and stirring rate of 240 rpm were applied continuously to a 50 mL PB electrolyte (0.01 M). Different concentrations of H_2O_2 were added to the PB solution at intervals of 30 s to analyse the sensitivities of dGN_{8V}, dGN_{4V}, and GO for HPRR. In the interference study, the times for the addition of 0.1 mM H_2O_2, 0.1 mM Glu, 0.1 mM AA, 0.1 mM DA, 0.1 mM UA, 0.1 mM H_2O_2, and again 0.1 mM H_2O_2 were 40, 80, 120, 160, 200, 240, and 280 s, respectively, after triggering the measurement. In the real sample experiments, the working electrode was fixed at -0.4 V for responding currents using various concentrations of 0.1 mL H_2O_2 in 4.9 mL milk solutions containing commercially available milk (0.9 mL) and 0.01 M PB solution (4 mL). The $KMnO_4$ titration method used to determine the concentration of H_2O_2 in the milk and samples in the real sample test is described in the supplementary material.
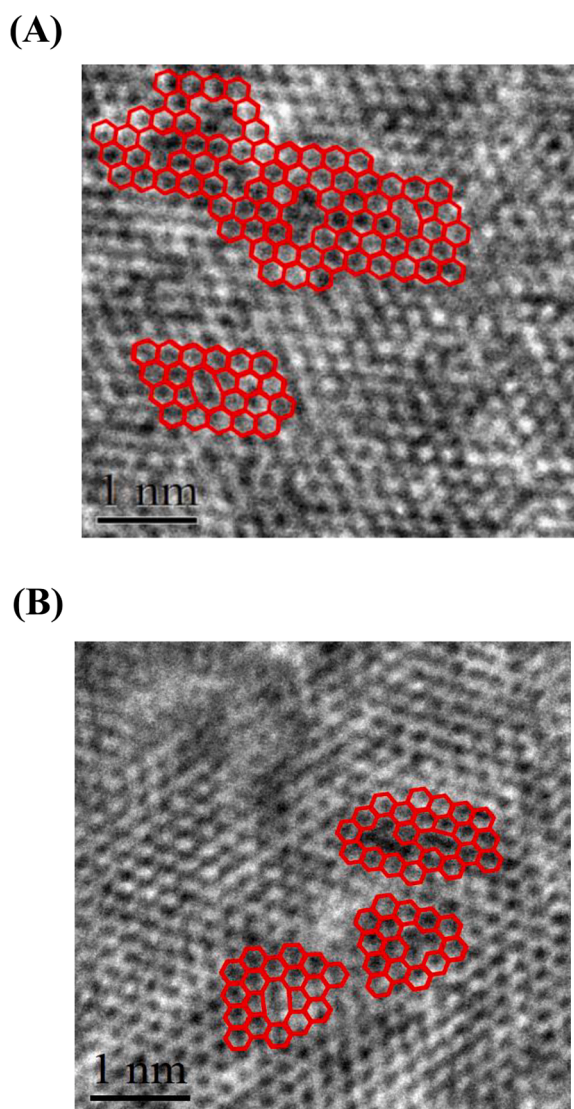
3. Results and discussion

3.1. Properties of dGN_{8V} and dGN_{4V}

The morphologies of dGN_{8V} and dGN_{4V} are displayed in the TEM images (Fig. 1A and 1B). In comparison to GO (Fig. 1C), dark areas are observed for the stacks and folds of the dGNs. Based on the dark areas, dGN_{8V} has more stacks and folds than dGN_{4V}. In addition to the few carbon dots produced (Fig. 1A) and the high intercalating current (Fig. S1), the violent intercalation of hydrogen phosphate ions and dihydrogen phosphate ions into the graphite electrode occurred under the synergistic effect of high intercalation potential (8 V) and ultrasonic radiation. As shown in Fig. S2, the yield for dGN_{8V} (1.75 mg) is 11.7 times greater than that for dGN_{4V} (0.15 mg). The amount obtained for dGN_{4V} is 7.5 times higher than the 0.02 mg obtained by the electrochemical method at the same applied potential. The effective throughput using the sonoelectrochemical method can be attributed to the rapid intercalation of phosphate ions between the graphitic layers and exfoliation under ultrasonic radiation.

A previous study reported point defects on dGN prepared by a sonoelectrochemical method with an applied potential of 2.997 V in order to intercalate SDS between the layers of a graphite electrode under a 240 W ultrasonic oscillator [8]. In contrast, spherical-aberration corrected field high-resolution TEM reveals 5-9, 5-8-5, and point defects on the dGN_{8V} (Fig. 2A) and dGN_{4V} (Fig. 2B), respectively. Interestingly, there are two double vacancies on dGN_{8V} (Fig. 2A) that are absent on dGN_{4V}. Typically, the terminal velocity of ions in the solution is proportional to the intensity of the applied potential between electrodes [15]. A rapidly expanding cavitation bubble can be formed under acoustic radiation in a sonoelectrochemical reaction [16]. The sudden asymmetric rupture of this cavitation bubble causes microjets to strike the dGN surface. Additionally, the rupture releases a significant amount of local heat (5000 K) from the gas zone in the bubble [17], which could break the sp^2 bond on dGN and form various vacancy defects (Fig. 2) on the surface. While several hydrogen phosphate and dihydrogen phosphate ions driven by the applied potential (8 V) are rapidly intercalated into the graphitic layer spacing, relatively fewer phosphate ions cover
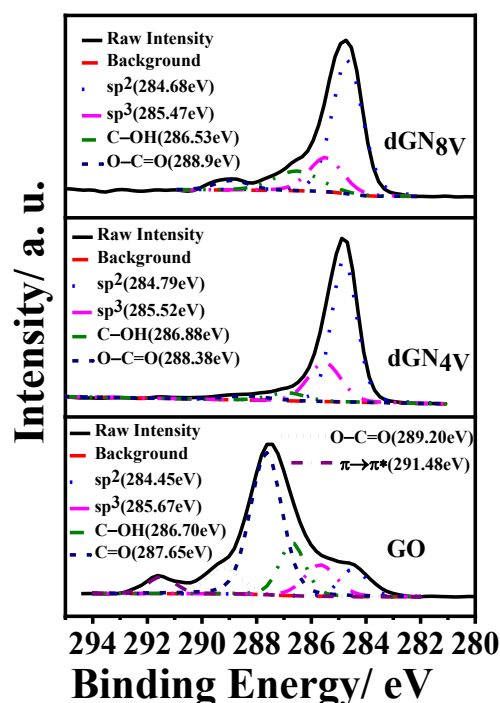
(A)

(B)

Fig. 2. High-resolution images of (A) dGN_{8V} and (B) dGN_{4V}, measured using spherical-aberration corrected field TEM.

Fig. 3. C 1 s XPS spectra for dGN_{8V}, dGN_{4V}, and GO.

Table 1

Compositions of dGN$_{8V}$, dGN$_{4V}$, and GO.

Sample	C (at %)						O (at %)
	sp^2	sp^3	C–OH	C=O	O–C=O	$\pi \to \pi^*$	
dGN$_{8V}$	50.15	14.22	11.22	–	4.11	–	20.3
dGN$_{4V}$	56.08	19.65	4.58	–	2.99	–	16.7
GO	6.92	9.20	12.48	41.64	8.27	4.29	17.2

Table 2

A summary of the defects on the dGN$_{8V}$, dGN$_{4V}$, and GO by Raman measurements.

Sample	D band/ cm^{-1}	G band/ cm^{-1}	I_D/I_G	L_D/ nm	N_D/ μm^{-2}
dGN$_{8V}$	1350	1584	1.09	11.50	2406
dGN$_{4V}$	1350	1584	0.81	13.40	1786
GO	1353	1600	–	–	–

the dGN$_{8V}$ surface struck by microjets. This is a plausible explanation for the formation of the double vacancy (Fig. 2A) by the removal of two carbon atoms.

In addition to the presence of double vacancy defects, an improved number of oxygen-containing groups is observed for the dGN obtained under high potential. Fig. 3 shows the XPS high-resolution spectra of narrow scans from the C 1 s region for dGN$_{8V}$, dGN$_{4v}$, and GO after curve fitting using a Lorentzian–Gaussian function. The C 1 s peaks for dGN$_{4V}$ (284.79 and 285.52 eV) arise due to the sp^2 and sp^3 hybridised carbon, respectively [18]. The sp^2 and sp^3 C contents of the dGN$_{4V}$ are 56.08 and 19.65 at%, respectively (Table 1). The peak at 286.88 eV is assigned to C–OH [19,20] with a C content of 4.58 at%. In addition, significant carbon oxidation (O–C=O) results in a peak at 288.38 eV with 2.99 at% C content [20]. The oxygen-containing groups on the sonoelectrochemical dGNs are C–OH and O–C=O, whereas GO exhibits complex groups composed of C=O (287.65 eV) [20] along with C–OH and O–C=O (Fig. 3). The C=O on the GO (prepared using Hummer's method [21]) shows a C content of 41.64 at% (Table 1). When a potential of 8 V is applied for the preparation of dGN, the contents of C–OH and O–C=O are 11.22 and 4.11 at% respectively, higher than those observed for dGN$_{4V}$. The FTIR spectrum (Fig. S3) for dGN$_{8V}$ with dGN$_{4v}$ shows significant peaks at 1217 and 1382 cm^{-1} for the stretching and deformation vibrations of C-OH [22], respectively. The intense C=O stretching vibration of O–C=O is detected at 1717 cm^{-1} [22]. Simultaneously, as shown in Table 1, the dGN$_{8V}$ sample exhibits an O content of 20.3 at%, which is greater than 16.7 and 17.2 at% for dGN$_{4V}$ and GO, respectively. It is worth noting that the O–C=O groups are typically located at the edges of the dGN or the vacancy defects on dGN. The double vacancy defects (Fig. 2A) on its surface inevitably improve the content of O–C=O. Additionally, from the full width at half maximum of the peak at 24° in the XRD patterns (Fig. S4) and the Scherrer equation, the grain size of dGN$_{8V}$ is measured as 0.53 nm, which is slightly greater than 0.49 nm for dGN$_{4V}$. The peak location is consistent with that of the reduced GO [23].

Fig. 4 shows the Raman spectra of dGN$_{8V}$, dGN$_{4V}$, and GO. The dGN$_{8V}$ spectrum clearly shows two bands at 1350 and 1584 cm^{-1}, referred to as the D and G bands, respectively. The D band can be attributed to the defects resulting from the breathing modes of the six-membered rings [24], while the G band reflects the ordered graphite
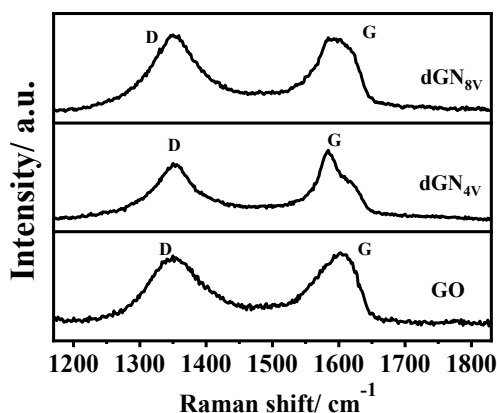

Fig. 4. Raman spectra of dGN$_{8V}$, dGN$_{4V}$, and GO.

structure from sp^2 hybridisation due to the doubly degenerate zone centre E$_{2g}$ mode [25]. The locations of the D and G bands for dGN$_{4V}$ are consistent with those seen in dGN$_{8V}$. The D and G bands of GO are measured at 1353 and 1600 cm^{-1}, respectively (Table 2). The G bands of the two dGNs are blue-shifted with respect to the typical location for highly ordered graphite (1580 cm^{-1}) [26]. These shifts can be attributed to the high frequency resonance of the isolated double bonds by the 5-8-5 vacancy and double vacancy defects on dGN$_{4V}$ and dGN$_{8V}$ [26].

Typically, the ratio of the intensities of the D and G peaks (I_D/I_G) represents the degree of defect density on the carbon sketch of dGN; however, it is unsuitable for the GO sample [24]. N_D, in terms of I_D/I_G, can be used to identify any improvement in the number of defects on the dGNs. It can be expressed by the following equations [27,38]:

$$L_D^2 = (1.8 \pm 0.5) \times 10^{-9} \lambda^4 (I_D/I_G)^{-1} \tag{1}$$

$$N_D = 10^{14}/(\pi L_D^2) \tag{2}$$

where L_D and λ are the distances between the defects and the laser wavelength (532 nm) used for the excitation in Raman spectroscopy, respectively. The L_D and N_D for dGN$_{4V}$ are 13.4 nm and 1786 μm^{-2}, respectively (Table 2). By increasing the applied potential, the N_D for dGN$_{8V}$ is further increased to 2406 μm^{-2}, which is 4.5 times greater than that of GN prepared by ultrasonication in an aqueous solution of cetyltrimethylammonium bromide (534.6 μm^{-2}) [27]; the L_D decreases to 11.5 nm. Thus, increasing the intercalating potential in the sonoelectrochemical method can improve the N_D on the dGN. As shown in the results of the N$_2$-adsorption/desorption isotherms (Fig. S5), a significant delay in N$_2$ desorption is observed for dGN$_{8V}$. The high N_D can cause strong N$_2$ adsorption on the dGN$_{8V}$. The specific surface areas obtained from the isotherms for dGN$_{8V}$ and dGN$_{4V}$ are 163.179 and 60.183 m$^2 \cdot$g^{-1}, respectively.

3.2. Catalysis of HPRR

Prior to the HPRR experiments, the ECSAs of dGN$_{8V}$, dGN$_{4V}$, and GO were estimated from the CV curves (Fig. S6) at different scan rates to measure the double-layer capacitance (Fig. S7) [28]. As shown in Table 3, the ECSAs of dGN$_{4V}$ and GO are 502.70 and 569.60 m$^2 \cdot$g^{-1}, respectively, both of which are smaller than the 1250.89 m$^2 \cdot$g^{-1} for dGN$_{8V}$. The mass activities (j_m) and specific activities (j_s) of dGN$_{8V}$ and dGN$_{4V}$ for the catalysis of HPRRs were investigated. Fig. 5A depicts the LSV curves of dGN$_{8V}$, dGN$_{4V}$, and GO in N$_2$-saturated 0.01 M PB solutions with and without 50 mM H$_2$O$_2$. When compared to the curves without H$_2$O$_2$, the CV curves with H$_2$O$_2$ clearly exhibit current reduction; thus, HPRR occurs on all the carbon catalysts, however, to a greater extent on the two dGN catalysts. It is worth noting that dGN$_{4V}$ with a small ECSA had a greater j_m than GO with a large ECSA. To determine the gain and cost factor of a catalyst, j_m can be expressed as

$$j_m = \frac{i_2 - i_1}{m} \tag{3}$$

where i_1 is the non-Faradaic current obtained in the PB solution without H$_2$O$_2$, i_2 is the cathodic current detected in the PB solution containing H$_2$O$_2$, and m is the loading weight of the carbon catalyst (14 μg). Fig. 5B shows the Tafel plots in terms of j_m for dGN$_{8V}$, dGN$_{4V}$, and GO. In contrast to GO, early rest potentials (E_rs) for the HPRR induced by

Table 3
E_{on}, i_1, i_2, ECSA, mass activity (j_m), and specific activity (j_s) for the catalysis of HPRR.

Sample	E_r/ V	Tafel slope at low η/ mV	Tafel slope at high η/ mV	i_1^a/ mA	i_2^b/ mA	ECSA/ m^2·g^{-1}	j_m^c/ mA·µg^{-1}	j_s^d/ µA cm^{-2}
dGN$_{8V}$	0.33	17.7	71.5	2.82×10^{-2}	2.11×10^{-1}	1250.89	1.31×10^{-2}	1.043
dGN$_{4V}$	0.34	20	64.5	1.80×10^{-2}	1.81×10^{-1}	502.70	1.17×10^{-2}	2.324
GO	0.15	25.6	47.8	1.25×10^{-3}	3.24×10^{-3}	569.60	1.42×10^{-4}	0.025

a. i_1 is the cathodic background current detected in 0.01 M PB solution without H_2O_2.

b. i_2 is the cathodic current detected in 0.01 M PB solution with 50 mM H_2O_2.

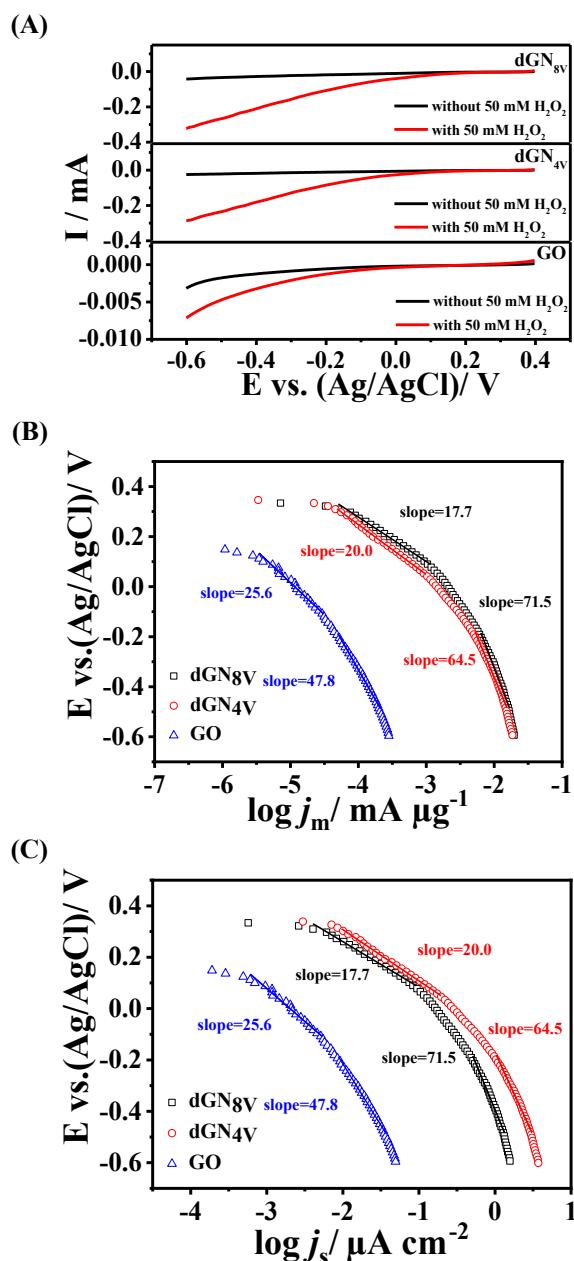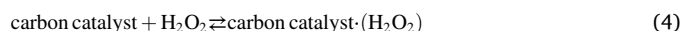c. $j_m = \dfrac{i_2 - i_1}{m}$

d. $j_S = \dfrac{i_2 - i_1}{ECSA}$

(A)

(B)

(C)

Fig. 5. Catalysis of HPRR: (A) LSV curves of dGN$_{8V}$, dGN$_{4V}$, and GO in N$_2$-saturated PB solutions with and without 50 mM H_2O_2; (B) Tafel plots of mass activities in terms of loading weight of dGN$_{8V}$, dGN$_{4V}$, and GO; (C) Tafel plots of specific activities in terms of ECSAs of dGN$_{8V}$, dGN$_{4V}$, and GO.

dGN$_{8V}$ and dGN$_{4V}$ were observed. The E_r value of dGN$_{8V}$ is 0.33 V (Table 3) and almost equal to that of dGN$_{4V}$ (0.34 V), while that of GO is 0.15 V. Thus, the HPRR easily occurs on the dGNs. Similar Tafel slopes (17.7–25.6 mV) are obtained for the three catalysts in the potential range 0.1 to −0.1 V, indicating that the coverage behaviour of H_2O_2 on these catalysts is similar under low overpotential. However, below −0.2 V, the slopes of the dGNs and GO differ significantly (71.5–64.5, and 47.8 mV, respectively). This can be attributed to the different adsorption behaviour of H_2O_2 on the surface containing vacancies and surface with oxygen-containing groups only. Typically, the reaction catalysed by a carbon catalyst can be explained as follows [29,30]:

$$\text{carbon catalyst} + H_2O_2 \rightleftarrows \text{carbon catalyst} \cdot (H_2O_2) \tag{4}$$

$$\text{carbon catalyst} \cdot H_2O_2 + e^- \rightarrow \text{carbon catalyst} \cdot (OH) + OH^- \tag{5}$$

$$\text{carbon catalyst} \cdot (OH) + e^- \rightarrow \text{carbon catalyst} + OH^- \tag{6}$$

An earlier study showed that the transfer of the first electron (Eq. (5)) is the rate-determining step [29]. However, herein, the slopes of 17.7–25.6 mV are much lower than −127 mV, suggesting the occurrence of Eq. (5). If the asymmetry parameter was 0.5 for the Tafel slopes [15] of the HPRR at 25 °C, these small slopes showed an electron number >5 and greater than 2 for Eqs. (5) and (6). This relationship suggests that the electron transfer to H_2O_{2ads} and OH^-_{ads} in these two electrochemical steps is not the rate-limiting step at low overpotentials. Thus, in addition to the significantly different E_r, the adsorption of H_2O_2 on the carbon catalysts can control the HPRR.

Fig. 5B and Table 3 show that the j_ms of dGN$_{8V}$ and dGN$_{4V}$ are 1.31×10^{-2} and 1.17×10^{-2} mA µg^{-1} at −0.4 V, respectively, while the j_m of GO is 1.42×10^{-4} mA µg^{-1}. Thus, dGN$_{8V}$ shows the best activity among the samples studied. Interestingly, dGN$_{4V}$ show a smaller ECSA but greater j_m than GO. The EIS results (Fig. S8) for the HPRR catalysis by these three dGN catalysts at −0.4 V further show that the diameter of the impedance arc increases in the order dGN$_{8V}$ < dGN$_{4V}$ < GO. The charge transfer resistances (R_{ct}) of dGN$_{8V}$ and dGN$_{4V}$ are 0.579 and 0.944 kΩ, respectively, while the R_{ct} of GO is 1.14 kΩ. The better activity of dGN$_{4V}$ compared to GO can be attributed to the lower R_{ct}, leading to the promotion of electron transfer for HPRR. Additionally, these sonoelectrochemical catalysts had high HPRR activities, as demonstrated by the data obtained from the CV curves at variable scan rates (Fig. S9). The relationship between the current (at −0.4 V) and the square root of the scanning rate for the HPRR in the presence of each of the catalysts is found to be linear (Fig. S10). Thus, the catalytic reactions at −0.4 V are H_2O_2-diffusion-controlled.

To study the origins of the active sites on these carbon catalysts, the j_s values were estimated. It can be expressed by

$$j_S = \frac{i_2 - i_1}{ECSA} \tag{7}$$

Fig. 5C shows the Tafel plots in terms of j_s for the catalysts studied. The slopes for HPRR in all cases are consistent with those for j_m in Fig. 5B, suggesting similar H_2O_2 adsorption and coverage on the catalyst. However, among these catalysts, dGN$_{4V}$ showed the best j_s at all
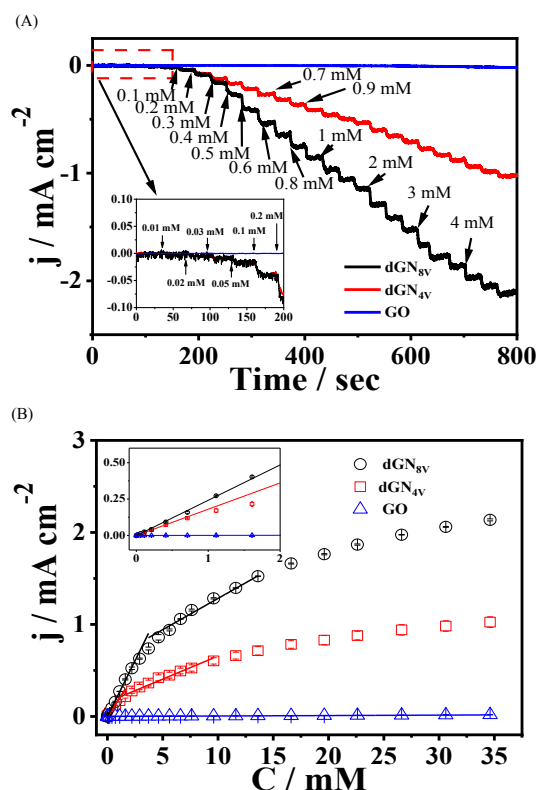
Fig. 6. H_2O_2 sensor: (A) amperometric current–time responses and (B) the corresponding calibration curves of dGN_{8V}, dGN_{4V}, and GO in N_2-saturated PB (0.01 M) solution after successive injections of different H_2O_2 concentrations at an applied potential of -0.4 V.

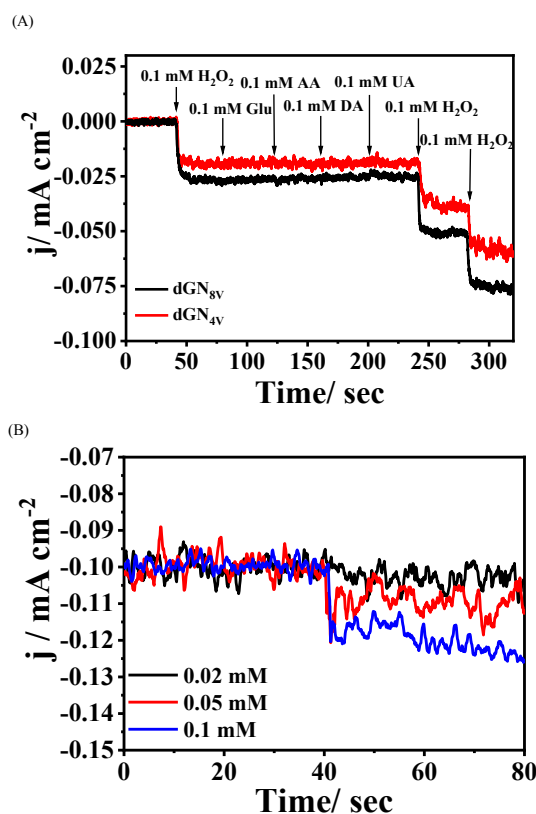**Fig. 7.** H_2O_2 sensor: (A) effect of interference from the current vs. time curves of H_2O_2 sensing of dGN_{8V} and dGN_{4V} at an applied potential of -0.4 V in 0.01 M PBS solution. (B) Current vs. time curves for dGN_{8V} as a H_2O_2 sensor in real samples.

applied potentials. At -0.4 V, the j_s value for dGN_{4V} is 2.324 $\mu A \cdot cm^{-2}$, which is greater than that for dGN_{8V} (1.043 $\mu A \cdot cm^{-2}$) and GO (0.025 $\mu A \cdot cm^{-2}$). As a result of the vacancy defects (Fig. 2), the activities of dGN_{4V} and dGN_{8V} are 93 and 41.7 times greater than that of GO, respectively. The higher j_s for dGN_{4V} compared with dGN_{8V} can be attributed to the low I_D/I_G (Table 2), leading to low ohmic resistance.

3.3. Non-enzymatic H_2O_2 sensors

The feasibility of dGN_{8V} and dGN_{4V} as non-enzymatic sensors was also tested because of their high j_m for H_2O_2. Fig. 6A shows the amperometric response to H_2O_2 catalysed by dGN_{8V}, dGN_{4V}, and GO at

an applied potential of -0.4 V. When H_2O_2 is added to the PB solution, the dGN_{8V} and dGN_{4V} catalysts exhibit significant cathodic current density responses, while GO is inactive. The current density was calculated from the current response over the geometric area (0.07 cm^2) of the GCE. At the initial measurement, the two dGN catalysts show a similar response to H_2O_2. The dGN_{8V} catalyst displays the most sensitive increase in current after 200 s when an aliquot of 0.3 mM H_2O_2 is added to the PB solution. As shown in Fig. 6B, a small deviation in the response currents of the carbon catalysts is highly repeatable, and the sensitivities and linear sensing ranges are obtained. The results are summarised in Table 4. The H_2O_2 sensitivities of dGN_{8V} in the linear concentration

Table 4

Figures of merit of reported catalysts on GCE for amperometric determination of H_2O_2 in PB or phosphate-buffered saline solutions at ~pH 7.

Catalysts	Applied potential/ V vs. Ag/AgCl	Linear range/mM	Sensitivity/$\mu A \cdot mM^{-1} \cdot cm^{-2}$	LOD/μM	Reference
Co^{III}-PPIX@Py_2CD^a	-0.3	0.001–10	–	0.25	[36]
PtNi/NCNF[b]	-0.1	0.00005–8	248.5	0.0375	[33]
rGox/AgNPs[c]	-0.4	0.002–20	236	0.73	[34]
		30–160	67		
AuNPs/$Fe_3O_4^d$	-0.5	0.001–1	266	0.108	[35]
defective few-layered graphene	-0.4	0.02–2.9	211.14	2.67	[37]
		2.9–11.6	57.43		
N-doped dGN	-0.4	0.01–2.225	231.3	0.88	[8]
dGN_{8V}	-0.4	0.01–4.61	243.08	2.31	This work
		4.61–13.61	66.75		
dGN_{4V}		0.01–2.21	180.65	4.87	
		2.21–9.61	44.48		
GO		0.01–34.61	0.478	78.23	

[a] per-O-methylated-cyclodextrin dimer with cobalt proto-porphyrin

[b] PtNi nanoparticles on N-doped carbon nanofiber

[c] silver nanoparticles-modified reduced graphene oxide

[d] Au nanoparticles mixed with Fe_3O_4 hybrids on carbon powders

Table 5

Real sample assays using dGN_{8V}/ GCE as amperometric sensor and compared with the $KMnO_4$ titration method for the detection of H_2O_2 with commercial milk/PB solution.

	Added (mM)	dGN_{8V}/ GCE as amperometric sensor			$KMnO_4$ titration		
		Detected/ mM	RSD/ %	Recovery/ %	Detected/ mM	RSD/ %	Recovery/ %
dGN_{8V}	0.02	0.019924	1.89	102.80	0.0205	1.15	102.00
	0.05	0.04913	2.52	98.26	0.0515	2.08	103.00
	0.1	0.098357	2.67	98.35	0.1025	1.04	102.50

a The RSD was obtained from the amounts of H_2O_2 determined in three independent measurements.

[b]$Recovery = \dfrac{Detected}{(Added H_2O_2 + diluted milk)}$; here, the concentration of the diluted milk with PB solution was 0.85 µM, which was calculated from the concentration of H_2O_2 in the original milk. The concentration of H_2O_2 in the milk was 4.72 µM, determined using the $KMnO_4$ titration method.

ranges 0.01–4.61 mM ($R^2 = 0.997$) and 4.61–13.61 mM ($R^2 = 0.996$) are 243.08 and 66.75 $\mu A \cdot mM^{-1} \cdot cm^{-2}$, respectively. The dGN_{4V} sample shows sensitivities of 180.65 and 44.48 $\mu A \cdot mM^{-1} \cdot cm^{-2}$ in the linear analysis range of 0.01–2.21 mM ($R^2 = 0.992$) and 2.21–9.61 mM ($R^2 = 0.985$), respectively. GO exhibited only one linear range (0.01–34.61 mM, $R^2 = 0.995$) with a sensitivity of 0.00042 $\mu A \cdot mM^{-1} \cdot cm^{-2}$. The order obtained for the sensitivity of the catalysts to H_2O_2 is $dGN_{8V} > dGN_{4V} > GO$. Based on the calibration curves in Fig. 6B and appropriate calculations [31], the limit of detection (LOD) [32] for dGN_{8V} is determined to be 2.31 µM at a signal-to-noise ratio of 3, which is lower than 4.87 µM for dGN_{4V} (Table 4). Thus, dGN_{8V} with double vacancy defects has comparable sensitivity to carbon-supported noble metal nanoparticles (NPs), for example, PtNi NPs [33], Ag NPs [34], and Au NPs/ Fe_3O_4 [35]. Its linear detection range is wider than that of PtNi NPs [33], Au NPs/Fe_3O_4 [35], and cyclodextrin dimer with cobalt proto-porphyrin (Co^{III}-PPIX@Py$_2$CD) [36]. Clearly, its j_m (Table 3) leads to sensitivity, which can be compared with that of metal nanoparticle sensors. The wide linear range of dGN_{8V} shows facial H_2O_2 adsorption and OH^- desorption on its surface without blocked active sites during HPRR. Additionally, when compared with defective, few-layered graphene [37] and N-doped dGN [8] prepared by the intercalation of SDS in sonoelectrochemical systems, the high sensitivity and wide linear analysis range of dGN_{8V} explicitly validates the present synthetic method for the feasibility of an H_2O_2 sensor.

Fig. 7A illustrates the comparable current–time curves for dGN_{8V} and dGN_{4V} at an applied potential of −0.4 V in a PB solution (0.01 M) with the sequential addition of 0.1 mM H_2O_2, 0.1 mM Glu, 0.1 mM AA, 0.1 mM DA, 0.1 mM UA, and 0.1 mM H_2O_2 (twice). Both catalysts show consistent current densities before and after the addition of interferences, demonstrating significant resistance to foreign substances and selective catalysis for H_2O_2 sensing and HPRR. In comparison to dGN_{4V}, dGN_{8V} shows high signals for H_2O_2. The dGN_{8V} sample was further investigated as a sensor using calibration curves (Fig. 6B) to determine the amount of H_2O_2 pollutant in commercially available milk. Fig. 7B shows the current density for milk samples mixed with 0.02, 0.05, and 0.1 mM H_2O_2. A high recovery and low relative standard deviation (RSD) are determined from the significant current responses for the three measurements, summarised in Table 5. The recoveries using dGN_{8V} as an H_2O_2 sensor are similar to the values obtained using the classical $KMnO_4$ titration method [33]. The data clearly demonstrate that the dGN_{8V} synthesised using the sonoelectrochemical method can be applied as sensors for H_2O_2 detection in milk samples.

4. Conclusions

The dGN_{4V} and dGN_{8V} samples with vacancy defects were successfully prepared by a sonoelectrochemical method in which an applied potential of 4 or 8 V propelled the intercalation of hydrogen phosphate and dihydrogen phosphate ions into a graphitic working electrode under ultrasonic oscillation at 640 W power and 37 kHz frequency. The dGN_{4V} thus obtained contained 5-9, 5-8-5, and point defects. In addition to these defects, double vacancies were also formed on the surface of the

dGN_{8V}, resulting in a high surface area and defect density. Investigation of the catalysis of HPRR indicated that the adsorption of H_2O_2 on the catalyst could be the rate-limiting step. The j_m of dGN_{8V} was significantly greater than that of dGN_{4V} and GO, whereas the dGN_{4V} had best j_s in terms of ECSA among these carbon catalysts. Furthermore, dGN_{8V} and dGN_{4V} showed reasonable current densities and high tolerance for foreign substances when they were applied as non-enzymatic H_2O_2 sensors. Real sample tests demonstrated the potential of dGN_{8V} as a sensor for the detection of H_2O_2 in milk.

CRediT authorship contribution statement

Tzu-Pei Wang: Investigation, Visualization, Formal analysis, Validation. **Chien-Liang Lee:** Methodology, Writing - review & editing, Supervision, Funding acquisition. **Chia-Hung Kuo:** Funding acquisition. **Wen-Cheng Kuo:** Funding acquisition.

Declaration of Competing Interest

The authors declare that they have no known competing financial interests or personal relationships that could have appeared to influence the work reported in this paper.

Appendix A. Supplementary data

Supplementary data to this article can be found online at https://doi.org/10.1016/j.ultsonch.2020.105444.

References

[1] Y. Jia, L. Zhang, A. Du, G. Gao, J. Chen, X. Yan, C.L. Brown, X. Yao, Defect graphene as a trifunctional catalyst for electrochemical reactions, Adv. Mater. 28 (43) (2016) 9532–9538, https://doi.org/10.1002/adma.201602912.

[2] M. Zhang, C. Choi, R. Huo, G.H. Gu, S. Hong, C. Yan, S. Xu, A.W. Robertson, J. Qiu, Y. Jung, Z. Sun, Reduced graphene oxides with engineered defects enable efficient electrochemical reduction of dinitrogen to ammonia in wide pH range, Nano Energy 68 (2020) 104323, https://doi.org/10.1016/j.nanoen.2019.104323.

[3] Y. Du, C. Jiang, W. Xia, L.i. Song, P. Li, B. Gao, C. Wu, L. Sheng, J. Ye, T. Wang, J. He, Electrocatalytic reduction of N 2 and nitrogen-incorporation process on

dopant-free defect graphene, J. Mater. Chem. A 8 (1) (2020) 55–61, https://doi.org/10.1039/C9TA10071G.

[4] P. Han, X. Yu, D.i. Yuan, M. Kuang, Y. Wang, A.M. Al-Enizi, G. Zheng, Defective graphene for electrocatalytic CO2 reduction, J. Colloid Interface Sci. 534 (2019) 332–337, https://doi.org/10.1016/j.jcis.2018.09.036.

[5] J.-H. Zhong, J. Zhang, X.i. Jin, J.-Y. Liu, Q. Li, M.-H. Li, W. Cai, D.-Y. Wu, D. Zhan, B. Ren, Quantitative correlation between defect density and heterogeneous electron transfer rate of single layer graphene, J. Am. Chem. Soc. 136 (47) (2014) 16609–16617, https://doi.org/10.1021/ja508965w.

[6] V.A. Kislenko, S.V. Pavlov, S.A. Kislenko, Influence of defects in graphene on electron transfer kinetics: The role of the surface electronic structure, Electrochim. Acta 341 (2020) 136011, https://doi.org/10.1016/j.electacta.2020.136011.

[7] B.G. Pollet, A short introduction to sonoelectrochemistry, Electrochem. Soc. Interface 27 (3) (2018) 41–42, https://doi.org/10.1149/2.F03183if.

[8] Y.-S. Wu, Z.-T. Liu, T.-P. Wang, S.-Y. Hsu, C.-L. Lee, A comparison of nitrogen-doped sonoelectrochemical and chemical graphene nanosheets as hydrogen peroxide sensors, Ultrason. Sonochem. 42 (2018) 659–664, https://doi.org/10.1016/j.ultsonch.2017.12.034.

[9] Y. Wang, Y.S. Xue, F. Huang, H. Zhang, K. Tao, R.R. Zhang, Q. Shen, H.L. Chang, A facile microfluidic hydrogen peroxide fuel cell with high performance: electrode interface and power-generation properties, ACS Appl. Energy Mater. 1 (2018) 5328–5335.

[10] E. Miglbauer, P.J. Wójcik, E.D. Głowacki, Single-compartment hydrogen peroxide fuel cells with poly(3,4-ethylenedioxythiophene) cathodes, Chem. Commun. 54 (84) (2018) 11873–11876, https://doi.org/10.1039/C8CC06802J.

[11] Y. Yang, H. Zhang, J. Wang, S. Yang, T. Liu, K. Tao, H. Chang, A silver wire aerogel promotes hydrogen peroxide reduction for fuel cells and electrochemical sensors, J. Mater. Chem. A 7 (18) (2019) 11497–11505, https://doi.org/10.1039/C9TA01963D.

[12] Y.H. Dong, J.B. Zheng, Environmentally friendly synthesis of Co-based zeolitic imidazolate framework and its application as H2O2 sensor, Chem. Eng. J. 392 (2020), 123690.

[13] F. Jiang, R. Yue, Y. Du, J. Xu, P. Yang, A one-pot 'green' synthesis of Pd-decorated PEDOT nanospheres for nonenzymatic hydrogen peroxide sensing, Biosens. Bioelectron. 44 (2013) 127–131, https://doi.org/10.1016/j.bios.2013.01.003.

[14] X.R. Chen, J. Gao, G.Q. Zhao, C. Wu, In situ growth of FeOOH nanoparticles on physically-exfoliated graphene nanosheets as high performance H2O2 electrochemical sensor, Sens. Actuat. B Chem. 313 (2020), 128038.

[15] C.H. Hamann, A. Hamnett, W. Vielstich, Electrochemistry, second ed., Wiley-Vch, Weinheim, 2007.

[16] T.J. Mason, V.S. Bernal, An introduction to sonoelectrochemistry in: B.G. Pollet (Ed.) Power Ultrasound in Electrochemistry, Wiely Chichester, 2012, p. 344.

[17] K.S. Suslick, D.A. Hammerton, R.E. Cline, Sonochemical hot spot, J. Am. Chem. Soc. 108 (18) (1986) 5641–5642, https://doi.org/10.1021/ja00278a055.

[18] R. Haerle, E. Riedo, A. Pasquarello, A. Baldereschi, sp2/sp3 hybridization ratio in amorphous carbon from C 1s core-level shifts: X-ray photoelectron spectroscopy and first-principles calculation, Phys. Rev. B 65 (2002), 045101.

[19] W. Li, X.-Z. Tang, H.-B. Zhang, Z.-G. Jiang, Z.-Z. Yu, X.-S. Du, Y.-W. Mai, Simultaneous surface functionalization and reduction of graphene oxide with octadecylamine for electrically conductive polystyrene composites, Carbon 49 (14) (2011) 4724–4730, https://doi.org/10.1016/j.carbon.2011.06.077.

[20] D. Yang, A. Velamakanni, G. Bozoklu, S. Park, M. Stoller, R.D. Piner, S. Stankovich, I. Jung, D.A. Field, C.A. Ventrice Jr., R.S. Ruoff, Chemical analysis of graphene oxide films after heat and chemical treatments by X-ray photoelectron and Micro-Raman spectroscopy, Carbon 47 (1) (2009) 145–152, https://doi.org/10.1016/j.carbon.2008.09.045.

[21] W.S. Hummers, R.E. Offeman, Preparation of graphitic oxide, J. Am. Chem. Soc. 80 (1958) 1339-1339.

[22] Z. Fan, J. Wang, Z. Wang, H. Ran, Y. Li, L. Niu, P. Gong, B. Liu, S. Yang, One-pot synthesis of graphene/hydroxyapatite nanorod composite for tissue engineering, Carbon 66 (2014) 407–416, https://doi.org/10.1016/j.carbon.2013.09.016.

[23] J.L. Zhang, H.J. Yang, G.X. Shen, P. Cheng, J.Y. Zhang, S.W. Guo, Reduction of graphene oxide via L-ascorbic acid, Chem. Commun. 46 (2010) 1112–1114.

[24] S. Eigler, C. Dotzer, A. Hirsch, Visualization of defect densities in reduced graphene oxide, Carbon 50 (10) (2012) 3666–3673, https://doi.org/10.1016/j.carbon.2012.03.039.

[25] A.C. Ferrari, J.C. Meyer, V. Scardaci, C. Casiraghi, M. Lazzeri, F. Mauri, S. Piscanec, D. Jiang, K.S. Novoselov, S. Roth, A.K. Geim, Raman spectrum of graphene and graphene layers, Phys. Rev. Lett. 97 (18) (2006), https://doi.org/10.1103/PhysRevLett.97.187401.

[26] K.N. Kudin, B. Ozbas, H.C. Schniepp, R.K. Prud`homme, I.A. Aksay, R. Car, Raman spectra of graphite oxide and functionalized graphene sheets, Nano Lett. 8 (1) (2008) 36–41, https://doi.org/10.1021/nl071822y.

[27] Z.F. Wang, J.J. Liu, W.X. Wang, H.R. Chen, Z.H. Liu, Q.K. Yu, H.D. Zeng, L.Y. Sun, Aqueous phase preparation of graphene with low defect density and adjustable layer, Chem. Commun. 49 (2013) 10835–10837.

[28] P. Wu, P. Du, H. Zhang, C. Cai, Microscopic effects of the bonding configuration of nitrogen-doped graphene on its reactivity toward hydrogen peroxide reduction reaction, Phys. Chem. Chem. Phys. 15 (18) (2013) 6920, https://doi.org/10.1039/c3cp50900a.

[29] S.J. Amirfakhri, D. Binny, J.-L. Meunier, D. Berk, Investigation of hydrogen peroxide reduction reaction on graphene and nitrogen doped graphene nanoflakes in neutral solution, J. Power Sources 257 (2014) 356–363, https://doi.org/10.1016/j.jpowsour.2014.01.114.

[30] T. Zhang, Y. Gu, C. Li, X. Yan, N. Lu, H.e. Liu, Z. Zhang, H. Zhang, Fabrication of Novel Electrochemical Biosensor Based on Graphene Nanohybrid to Detect H 2 O 2 Released from Living Cells with Ultrahigh Performance, ACS Appl. Mater. Interfaces 9 (43) (2017) 37991–37999, https://doi.org/10.1021/acsami.7b14029.s001.

[31] X. Mao, X. Yang, G.C. Rutledge, T. Alan Hatton, Ultra-Wide-Range Electrochemical Sensing Using Continuous Electrospun Carbon Nanofibers with High Densities of States, ACS Appl. Mater. Interfaces 6 (5) (2014) 3394–3405, https://doi.org/10.1021/am405461j.

[32] E. Desimoni, B. Brunetti, Presenting Analytical Performances of Electrochemical Sensors. Some Suggestions, Electroanalysis 25 (7) (2013) 1645–1651, https://doi.org/10.1002/elan.201300150.

[33] H. Guan, Y. Zhao, J. Zhang, Y. Liu, S. Yuan, B. Zhang, Uniformly dispersed PtNi alloy nanoparticles in porous N-doped carbon nanofibers with high selectivity and stability for hydrogen peroxide detection, Sens. Actuators, B 261 (2018) 354–363, https://doi.org/10.1016/j.snb.2018.01.169.

[34] P. Salazar, I. Fernández, M.C. Rodríguez, A. Hernández-Creus, J.L. González-Mora, One-step green synthesis of silver nanoparticle-modified reduced graphene oxide nanocomposite for H2O2 sensing applications, J. Electroanal. Chem. 855 (2019), 113638.

[35] H. Liu, Q. Chen, X. Cheng, Y. Wang, Y. Zhang, G. Fan, Sustainable and scalable in-situ fabrication of Au nanoparticles and Fe3O4 hybrids as highly efficient electrocatalysts for the enzyme-free sensing of H2O2 in neutral and basic solutions, Sens. Actuat. B Chem. 314 (2020), 128067.

[36] M.F. Fan, H.M. Wang, L.J. Nan, A.J. Wang, X. Luo, P.X. Yuan, J.J. Feng, The mimetic assembly of cobalt prot-porphyrin with cyclodextrin dimer and its application for H2O2 detection, Anal. Chim. Acta 1097 (2020) 78–84.

[37] S.-Y. Hsu, C.-L. Lee, Sonoelectrochemical exfoliation of highly oriented pyrolytic graphite for preparing defective few-layered graphene with promising activity for non-enzymatic H2O2 sensors, Microchim Acta 184 (7) (2017) 2489–2496, https://doi.org/10.1007/s00604-017-2297-x.

[38] L.G. Cancado, A. Jorio, E.H.M. Ferreira, F. Stavale, C.A. Achete, R.B. Capaz, M.V.O. Moutinho, A. Lombardo, T.S. Kulmala, A.C. Ferrari, Quantifying defects in graphene via raman spectroscopy at different excitation energies, Nano Lett. 11 (2011) 3190–3196, https://doi.org/10.1021/nl201432g.